SCHOOL OF ENGINEERING AND DESIGN

TECHNISCHE UNIVERSITÄT MÜNCHEN

Master's Thesis in Earth Oriented Space Science and Technology (ESPACE)

Ionosphere and Ground Motion Estimation from Azimuth Subbands

Colin Moldenhauer

SCHOOL OF ENGINEERING AND DESIGN

TECHNISCHE UNIVERSITÄT MÜNCHEN

Master's Thesis in Earth Oriented Space Science and Technology (ESPACE)

Ionosphere and Ground Motion Estimation from Azimuth Subbands

Schätzung der Ionosphäre und Bodenbewegung aus Azimuth-Subbändern

Author:	Colin Moldenhauer
Advisor:	Dr. Giorgio Gomba
Supervisor:	Prof. Dr. Marco Körner
Submission Date:	09.03.2025

I confirm that this Master's Thesis in Earth Oriented Space Science and Technology (ESPACE) is my own work and I have documented all sources and material used.

Munich, 09.03.2025

Colin Moldenhauer

Abstract

SAR based estimation of glacial motion is a key tool to globally monitor the effects of climate change on the cryosphere. Glacial movement between two observations is measured via cross-correlation, but azimuth offsets are biased by shifts of the SAR impulse response due to linear variations of the ionosphere along the azimuth direction. Due to increased sensitivity of higher-wavelength systems to the ionosphere, the next generation of L-band earth observation missions requires the precise estimation of the differential ionospheric state and subsequent compensation of ionospheric azimuth shifts. In particular, we require turbulent ionospheric components to be recovered and compensated, due to their large contribution to azimuth offset biases. However, current estimation methods are not able to reconstruct high-frequency ionospheric perturbations as a result of smoothing or are sensitive to both azimuth ground motion and ionosphere and thus can not separate the two effects. The second derivative of the azimuth phase history allows to separate azimuth ground motion from ionospheric effects, providing additional information on the ionospheric state. In this thesis, we investigate the improved estimation of the differential ionospheric phase screen from three azimuth subbands in combination with split-spectrum measurements. Using simulated data, we show that three azimuth subbands enable the recovery of high-frequency ionosphere even in the presence of strong azimuth ground motion.

Contents

1. Introduction

Ionosphere estimation Ionospheric effects disturb the observation of geophysical processes by means of interferometric SAR (InSAR). In order to improve the measurement precision, the ionosphere needs to be estimated and its effect compensated. The ionosphere correction is of particular importance for the imminent L-band missions *NISAR* (NASA-ISRO) and *ROSE-L* (ESA) due to the increased influence of the ionosphere on low-wavelength systems. This thesis is mainly concerned with two effects of the ionosphere: the phase advance caused by the total electron content (TEC) and the modification of the azimuth impulse response caused by a linear slope of the TEC within the synthetic aperture.

The *split-spectrum method* is commonly used to estimate the differential ionosphere from InSAR data, but due to large noise amplification and the necessary consecutive filtering step, the spatial resolution of the estimate is limited. Small-scale ionospheric variations hence can not be recovered by this method.

The first derivative of the differential phase in azimuth direction may be used to introduce additional information to the estimation to recover high-frequency ionosphere [GD17]. The derivative can be estimated from the interferometric data itself, either through patch-based cross-correlation, or by forming two azimuth subbands, as used in this thesis. Both methods however are biased by the presence of azimuth ground motion between the observations and thus only correctly estimate the ionosphere in the absence of azimuth ground motion. The estimation from two azimuth subbands can be extended to three subbands, which allows to compute the second derivative of the azimuth phase history, separating azimuth ground motion and ionospheric shifts. Reducing ionospheric shifts improves the precision of downstream applications that rely on unbiased azimuth offsets. One possible use case of the improved estimation, namely improved estimation of glacial flow velocities, is presented in the following.

Measurement of glacial motion The cryosphere is an important component of the earth's climate system. Since 1992, $0.59 \pm 0.02\,\mathrm{mm/yr}$ of sea level rise can be attributed to the polar ice sheets of Greenland, East Antarctica, West Antarctica, and the Antarctic Peninsula combined [She+12]. Ice mass loss in Greenland has accelerated from $39 \pm 41\,\mathrm{Gt/yr}$ between 1992 and 1999 to $243 \pm 47\,\mathrm{Gt/yr}$ between 2010 and 2019 [Fox+21]. Ice discharge via Greenland's outlet glaciers is one of the major ice mass loss processes. Between 2009 and 2012, it accounted for 32 % of ice mass loss [End+14]. In light of temporal fluctuations of the acceleration of marine-terminating glaciers, continuous observation at high revisit frequencies is required to better comprehend the glaciers' impact on sea level rise [Lem+18], which is possible with spaceborne synthetic aperture radar (SAR). Dynamic processes can be observed on short timescales due to revisit times of six days of the Sentinel-1 constellation. Next generation L-band systems promise improved observation capabilities due to larger penetration depth and thus reduced impact of surface decorrelation, e.g. by snow accumulation. Glacial flow is measured by means of offset tracking methods, where the ground movement between two observations is determined via patch-based cross-correlation. An example output of the method is shown in Figure 1.1, where yearly measurements have been combined to produce a ice flow velocity map of Greenland. The impact of the ionospheric error component relative to other error sources increases with shorter temporal baseline. Thus, in order to be able to resolve high-frequency geophysical signals, the compensation of ionospheric errors becomes a priority.

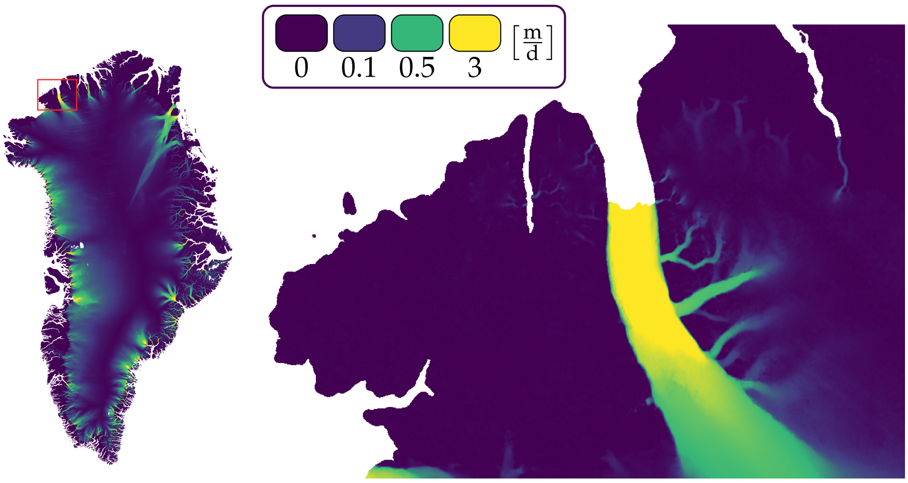

(a) Greenland

(b) Petermann Glacier

Figure 1.1.: Glacial flow velocity map of Greenland in meters per day, obtained from S1 observations averaged over one year. Glaciers move up to three meter per day (yellow), while bedrock remains stable (dark purple). The right subplot shows a crop of the Petermann Glacier, which is used as a reference to model azimuth ground motion in this thesis. Data by enveo.

Ionosphere over Greenland Ionospheric effects are a common source of uncertainty over the glaciers of Greenland and hinders the offset tracking between two observations. Figure 1.2a shows the azimuth shifts over central Greenland measured via cross-correlation from a pair of Sentinel-1 observations. Close to zero glacial motion is present in the imaged area, thus, the observed shifts are caused by ionosphere. For C-band, the shifts amount to more than two meters. Observed with L-band, the ionospheric shits would be 20 times stronger [Gom16].

Figure 1.2b visualizes the superposition of glacial and ionospheric azimuth shifts. The glacial motion can be observed in the image center as the dark red homogeneous area,

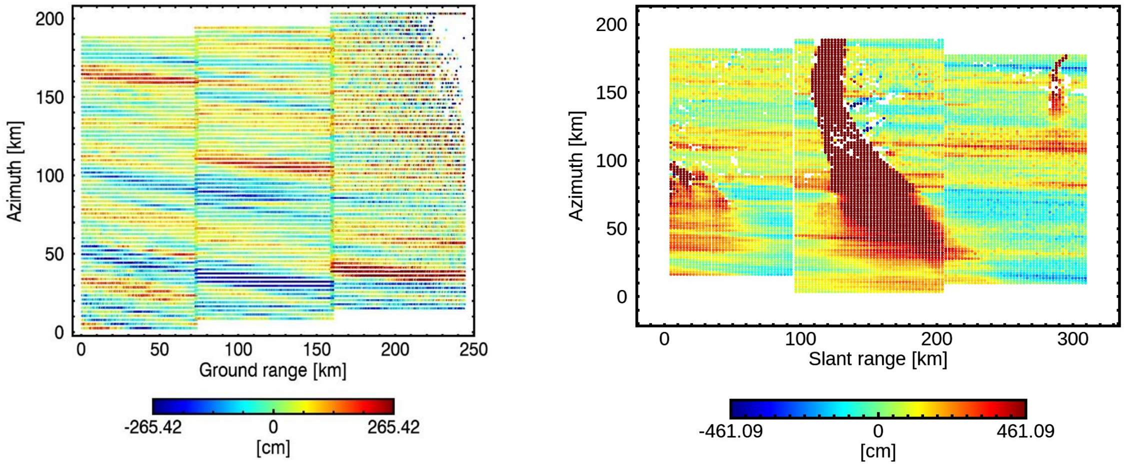

(a) Ionospheric shifts

(b) Ground and ionospheric shifts

Figure 1.2.: **(a)** Ionospheric azimuth shifts over Greenland measured by patch-based cross-correlation. From [Gom]. **(b)** Superposition of glacial and ionospheric shifts. The colorbar is truncated; glacial shifts exceed five meters.

while ionospheric shifts take the form of horizontal streaks. The two effects can not be separated with current methods, calling for the development of a new method that is capable of estimating high-frequency ionosphere without the bias of ground motion.

2. Ionosphere and SAR

This chapter presents the theoretical background, characterizing the properties of the ionosphere and its effects on SAR. The core principals of radar remote sensing with SAR and InSAR are summarized. The split-spectrum method and beam splitting in azimuth direction are explained in more detail, as they are central to the method presented in this thesis.

2.1. Ionosphere

The ionosphere is the part of the upper atmosphere characterized by the presence of ionized particles, spanning atmospheric heights from 60 km to 1000 km, with peak intensities occurring between 300 and 400 km [Dav90]. While the true intensity distribution of ionization is grouped into multiple layers, it is commonly modeled as a single thin layer at an ionospheric height H_i over the earth surface. The ionosphere's strength is quantified by the total electron content (TEC), defined as the integrated density of free electrons along a path. One needs to distinguish the vertical TEC (i.e. integrated along the local surface normal of the earth) from the slant TEC (i.e. integrated along a slanted propagation path as for SAR). If not specified otherwise, we refer to the slant TEC as TEC.

The intensity of the ionosphere varies both spatially and temporally. The solar radiation drives the ionization of the atmosphere. Therefore, the day-night cycle, the seasons and the solar cycle affect the state of the ionosphere. In auroral regions, the solar wind and the earth magnetic field are additional factors. Under norm conditions, the global spatial distribution of the ionosphere is dominated by the sun zenith angle. The highest ionospheric intensity occurs in regions of local noon, as illustrated by Figure 2.1. The most prominent large-scale deviation is the equatorial anomaly, referring to peak intensities occurring at latitudes about $\pm$ 15° with respect to the magnetic equator. Further, *traveling ionospheric disturbances* can produce medium-scale (hundreds of kilometers) to large-scale (thousands of kilometers) anomalies in the electron density [Her+11]. In equatorial and auroral regions, additional small scale irregularities, down to the meter level, can be present, termed *scintillation* [Dav90].

2.2. SAR & InSAR

SAR is a remote sensing technique generating a two-dimensional observation of the ground, using the echo of electromagnetic pulses emitted by the radar. Along the

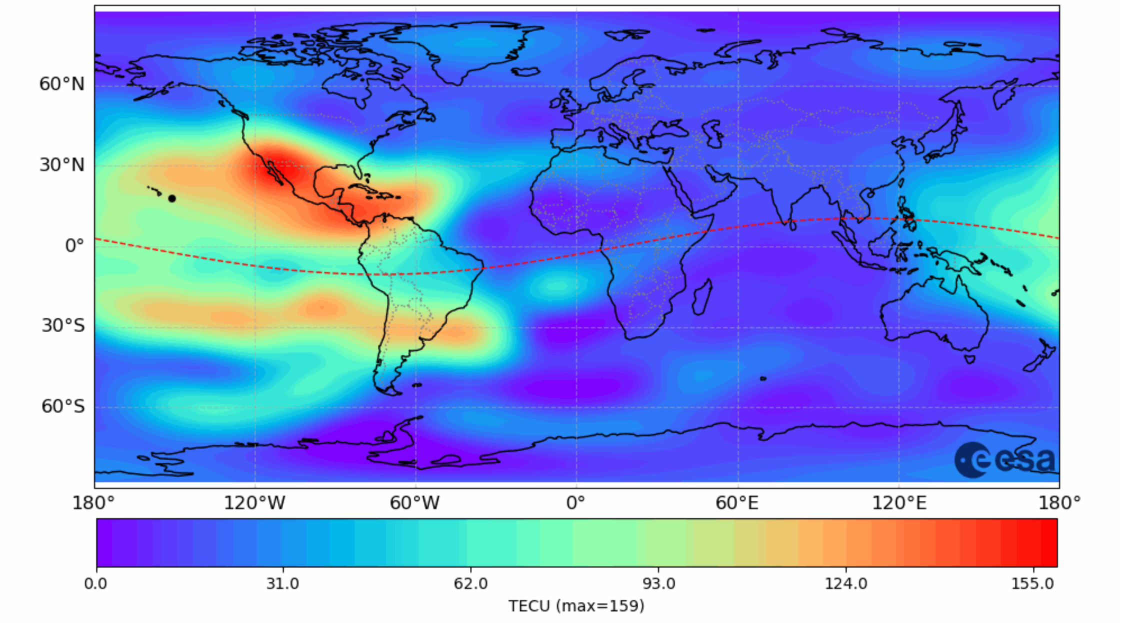

Figure 2.1.: Global TEC map on 2024-05-10 at 22:00 (UTC). Figure provided by ESA's Navigation Support Office. High ionosphere intensity can be observed in areas of local noon (e.g. North America). The dashed red line indicates the geomagnetic equator.

system's line of sight (LOS), the distance of scatterers to the sensor is measured on the basis of signal flight time. A high azimuth (along-track) resolution is achieved by synthesizing a large aperture through combination of consecutive pulses along the direction of travel.

By means of InSAR, differences between two observations of the same ground scene taken at different times or from different positions are quantified, leveraging the sensitivity of the differential phase to small distance changes. The phase difference $\Delta\Phi$ between the two observations contains contributions from LOS ground movement $\Delta\Phi_{mov,rg}$, topography $\Delta\Phi_{topo}$, differential troposphere $\Delta\Phi_{tropo}$ and differential ionosphere $\Delta\Phi_{iono}$, i.e.

$$\Delta\Phi = \Delta\Phi_{mov,rg} + \Delta\Phi_{topo} + \Delta\Phi_{tropo} + \Delta\Phi_{iono}. \tag{2.1}$$

2.3. Ionospheric Effects on SAR

The presence of free electrons in the ionosphere influences the propagation of radio waves as a result of the non-nominal refraction index of ionospheric plasma [Dav90]. The group velocity of a radio pulse is reduced, causing range distances to be overestimated. Conversely, the measured phase is advanced by

$$\Delta\Phi_{iono} = -\frac{4\pi K}{c f_0} TEC, \tag{2.2}$$

where $K \approx 40.31 \frac{m^3}{s^2}$, c is speed of light, f_0 the SAR system carrier frequency and TEC the TEC along the LOS. With lower frequency, the influence of the ionosphere on the phase increases.

Azimuth shifts A linear azimuth profile of the TEC causes a shift of the impulse response proportional to the slope of the linear ionosphere within the synthetic aperture. The TEC (here denoted as Ψ) along the azimuth coordinate η can be decomposed into a constant term, a linear term and higher-order terms:

$$\Psi(\eta) = \Psi_0 + \Psi_1 \eta + \mathcal{O}(\eta^2). \tag{2.3}$$

Neglecting higher-order terms, the azimuth shift caused by the ionspheric slope $\Delta\eta_{iono}$ is given as

$$\Delta\eta_{iono} = \frac{vH_i}{2\pi K_a H} \Psi_1 = -\frac{KRH_i}{f_0^2 vH} \Psi_1, \tag{2.4}$$

with the linear orbit FM rate K_a, the broadside range R, orbit velocity v and satellite height H [Gom16].

2.4. Ionosphere Estimation

The ionosphere can be estimated from SAR data on the basis of different physical effects. Dispersive effects on the range signal can be used to estimate the differential TEC [Brc+10]. The change in polarization caused by Faraday rotation can be related to the TEC. However, the required fully polarimetric data is not widely available [Lia+24; Gom16]. Other methods exploit the blurring of the range signal, the group delay and phase advance caused by the differential ionosphere, or combinations of the methods. In the following, the (range) split-spectrum method and the (azimuth) subband-based estimation (also called *MAI* [BZ06], spectral diversity) of the ionosphere is explained in more detail.

2.4.1. Split-spectrum method

The *split-spectrum method* [Gom+16; RHC10; Brc+10] exploits the dispersive character of the ionospheric path delay to separate the ionospheric phase component from the non-dispersive components. To this end the interferometric phase of topography, LOS displacement and troposphere are grouped as the non-dispersive phase $\Delta\Phi_{nondisp}$. Equation 2.1 is then rewritten as

$$\begin{aligned} \Delta\Phi &= \Delta\Phi_{mov,rg} + \Delta\Phi_{topo} + \Delta\Phi_{tropo} && + \Delta\Phi_{iono} \\ &= \frac{4\pi f_0}{c}(\Delta r_{motion} + \Delta r_{topo} + \Delta r_{tropo}) && - \frac{4\pi K}{c f_0}\Delta TEC \\ &= \Delta\Phi_{nondisp} && + \Delta\Phi_{disp} \end{aligned} \tag{2.5}$$

For both the reference and secondary observation, the spectrum is split into a low range-subband and a high subband with center frequencies f_L and f_H respectively. The two interferograms for the new center frequencies are then

$$\begin{aligned}\Delta\Phi_L &= \frac{f_L}{f_0}\Delta\Phi_{nondisp} + \frac{f_0}{f_L}\Delta\Phi_{disp}\\ \Delta\Phi_H &= \frac{f_H}{f_0}\Delta\Phi_{nondisp} + \frac{f_0}{f_H}\Delta\Phi_{disp}.\end{aligned} \tag{2.6}$$

After solving the equations we obtain the estimators for the dispersive and non-dispersive components as

$$\begin{aligned}\Delta\hat{\Phi}_{disp} &= \frac{f_L f_H}{f_0(f_H^2 - f_L^2)}(\Delta\Phi_L f_H - \Delta\Phi_H f_L)\\ \Delta\hat{\Phi}_{nondisp} &= \quad\frac{f_0}{f_H^2 - f_L^2}\quad(\Delta\Phi_H f_H - \Delta\Phi_L f_L).\end{aligned} \tag{2.7}$$

Phase noise in the high and low range-subbands will be amplified by the large coefficients and needs to be filtered, thereby losing high-frequency information.

2.4.2. Azimuth subbands

Azimuth subbands are formed by splitting the azimuth spectrum, creating multiple sub-apertures [BZ06] (see Figure 2.2). The first azimuth derivative may be determined from differencing multiple azimuth subbands due to the spatial separation of the ionosphere. Using n subbands, the $n-1^{th}$ difference can be determined. [GD17] utilizes two subbands in order to

The resulting subbands image the same ground footprint, but at different squint angles, as illustrated by Figure 2.2. As a result, the subbands are subject to a different part of the ionosphere.

The phase difference observed in azimuth subband S is dependent on the ionospheric phase screen and azimuth ground motion. To investigate the effects of ionosphere and azimuth ground movement, range motion $\Delta\Phi_{mov,rg}$, topography phase $\Delta\Phi_{topo}$ and contributions $\Delta\Phi_{tropo}$ are considered to be zero, which yields

$$\begin{aligned}\Delta\Phi_S &= \Phi_{iono,S} \qquad\quad + \Delta\Phi_{\Delta az,S}\\ &= -\frac{4\pi K}{cf_0}\Delta TEC_S + 2\pi f_{D,S}\Delta\eta,\end{aligned} \tag{2.8}$$

with the subband's ionospheric phase screen ΔTEC_S and doppler centroid frequency $f_{D,S}$ and azimuth ground displacement $\Delta\eta$.

First azimuth derivative After computation of two azimuth subband interferograms, we can compute the first derivative of the azimuth phase history $\Delta\Phi_{az}$ as the difference of the two interferograms:

$$\begin{aligned} p_{az} \cdot \Delta\Phi_{az} &= \Delta\Phi_{S_2} - \Delta\Phi_{S_1} \\ &= -\frac{4\pi K}{c f_0}(\Delta TEC_{S_2} - \Delta TEC_{S_1}) + 2\pi(\underbrace{f_{D,S_2} - f_{D,S_1}}_{f_{D,S_2}=-f_{D,S_1}})\Delta\eta \\ &= -\frac{4\pi K}{c f_0}\Delta I_{az} + 4\pi f_{D,S_2}\Delta\eta, \end{aligned} \tag{2.9}$$

where both sides of the equation were multiplied with the step size of the difference quotient, the azimuth pixel resolution p_{az}, for better readability.

If azimuth ground motion is present, the first azimuth derivative of the phase screen will be superimposed by the effect of the ground motion in azimuth direction. Hence, inversion and therefore integration of ΔI_{az} will yield a biased result.

Second azimuth derivative Splitting the azimuth spectrum into three subbands (forward-looking, broadside, backward-looking) with a third of the original azimuth bandwidth, allows to compute the second discrete derivative of the azimuth phase history $\Delta^2\Phi_{az}$. Note that the difference quotient has been multiplied by the denominator $2p_{az}^2$ to avoid clutter. The resulting double difference yields:

$$\begin{aligned} 2p_{az}^2 \cdot \Delta^2\Phi_{az} &= (\Delta\Phi_{S_3} - \Delta\Phi_{S_2}) - (\Delta\Phi_{S_2} - \Delta\Phi_{S_1}) = \Delta\Phi_{S_3} - 2\Delta\Phi_{S_2} + \Delta\Phi_{S_1} \\ &= -\frac{4\pi K}{c f_0}(\Delta TEC_{S_3} - 2\Delta TEC_{S_2} + \Delta TEC_{S_1}) \\ &\quad + 2\pi(f_{D,S_3} - 2\underbrace{f_{D,S_2}}_{=0} + f_{D,S_1})\Delta\eta \\ &= -\frac{4\pi K}{c f_0}\Delta^2 I_{az} + 2\pi\underbrace{(f_{D,S_3} + f_{D,S_1})}_{=0}\Delta\eta \\ &= -\frac{4\pi K}{c f_0}\Delta^2 I_{az}. \end{aligned} \tag{2.10}$$

The azimuth ground motion contribution cancels due to the opposite sign of the forward-looking and backward-looking subbands' doppler centroid frequencies. What remains is the second azimuth derivative of the ionospheric phase screen, which yields the potential for high-frequency components of the ionosphere to be recovered.

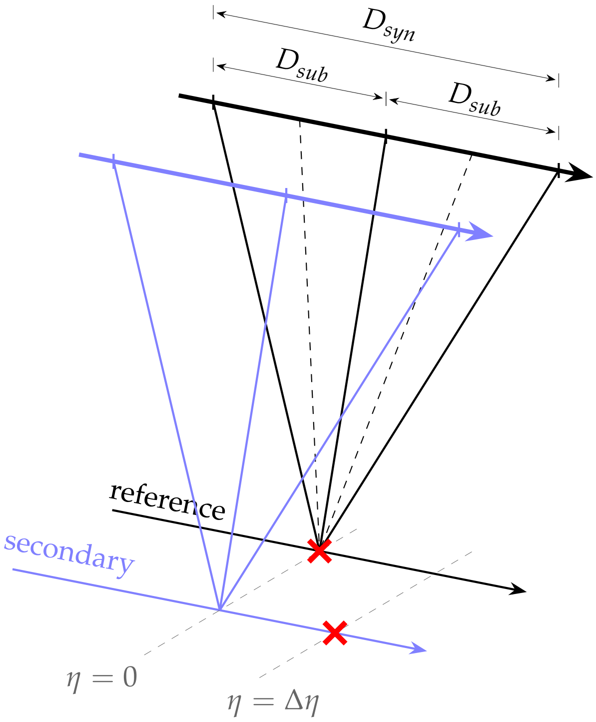

Figure 2.2.: Differential observation geometry for reference and secondary acquisitions. The imaged ground footprint remains the same, however the target, initially at $\eta = 0$, has moved in the alongtrack direction by $\Delta\eta$ between acquisitions.

3. Method

This chapter describes the method used for evaluating the application of azimuth subbands for improved ionosphere and ground movement estimation. The data simulation and formulation of the estimation problem are explained, followed by an overview of the conducted experiments.

3.1. Simulation

For the purpose of quality assessment of the estimation methods, the differential ionospheric state $I(x, y)$ and azimuth ground motion $G(x, y)$ between observations is simulated. Both fields are modelled to resemble the real-world phenomena explained in Figure 1.2. Given this ground truth scenario as input, an estimate of the ionospheric phase screen as obtained by the split-spectrum method is simulated as the true ionosphere superimposed by normal phase estimation noise. Additionally, azimuth subbands are simulated as shifted observations of the true ionospheric phase screen, further influenced by the azimuth ground motion. The azimuth derivative is then computed from the subbands. A schematic overview of the simulation pipeline can be found in Figure 3.1. In the following, the implementation of the simulation submodules is explained in more detail.

3.1.1. Simulation parameters

The simulation pipeline depends on a number of parameters, which can be grouped into SAR system specific parameters, scene parameters and observation parameters. The response of a SAR system depends on its frequency and bandwidth, the physical antenna size and the orbit altitude. The parameters of the future L-band system *NISAR* are used for reference. The grid of the simulated observable ionosphere is specified through the extent in azimuth and range direction and the respective cell resolutions in both spatial directions. Further variables influencing the InSAR observation are the height of the ionosphere and coherence of the image pair. The values used for simulation are specified in Table 3.1.

3.1.2. Ionospheric state

The observable low-pass ionosphere $I(x, y)$ is simulated on a raster of height $h = d_{az}/\Delta_{az}$ and width $w = d_{rg}/\Delta_{rg}$ as the sum of two-dimensional sinusoidals ξ_i of different amplitudes, wavelengths and orientations, i.e.

name	description	value
SAR parameters		
f_0	center frequency	1.257 GHz
D	antenna physical length	12 m
H	orbit height	747 km
α	look angle	40°
B	bandwidth	20 MHz
scene parameters		
l_{az}	azimuth image extent	200 km
l_{rg}	range image extent	250 km
p_{az}	azimuth resolution	3 km
p_{rg}	range resolution	1 km
observation parameters		
γ	coherence	0.6
H_i	ionosphere layer height	350 km

Table 3.1.: Simulation parameters grouped by SAR parameters, scene parameters and observation parameters. SAR parameters are chosen to resemble those of *NISAR-L*

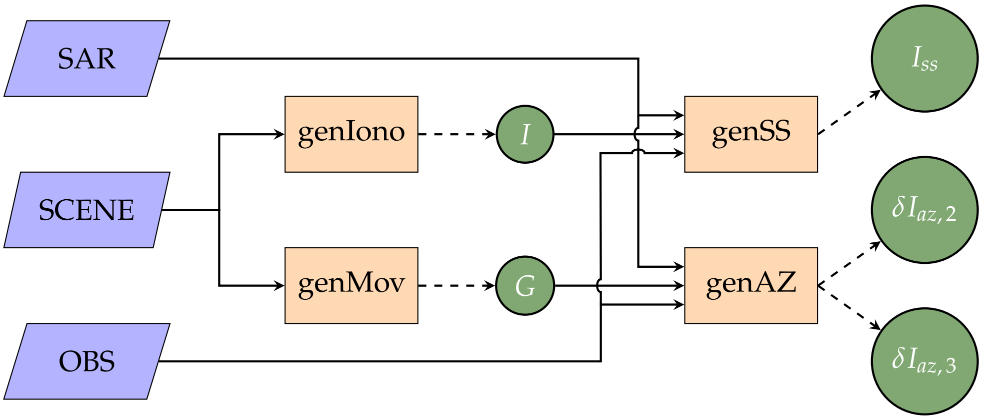

Figure 3.1.: Simulation workflow. Blue trapezoids represent parameter settings defining the simulation (see Table 3.1). Orange rectangles are simulation processes that generate data (green circles). Small circles indicate intermediate data, which is not directly used in the estimation, but as inputs to downstream simulation processes. The large circles represent the simulated data used as inputs to the estimation, in other words, they simulate the data that could be extracted from SAR measurements. The suffix *SS* corresponds to the (simulated) split-spectrum method, while *AZ* or *az* indicate quantities derived from azimuth subbands.

$$I(x,y) = I_0 + \sum_i m_i(x,y)\, \xi_i(x,y), \tag{3.1}$$

on $0 \le x \le w$, $0 \le y \le h$ and with mask $0 \le m_i \le 1$, allowing for local addition of high-frequency ionosphere. Each sinusoidal is defined as

$$\xi_i(x,y;A_i,\lambda_i,\theta_i) = A_i \cos\left(\frac{2\pi}{\lambda_i}\left\langle \begin{bmatrix} x \\ y \end{bmatrix}, \begin{bmatrix} \sin(\theta_i) \\ \cos(\theta_i) \end{bmatrix} \right\rangle\right), \tag{3.2}$$

with amplitude A_i, wavelength λ_i and rotation angle θ_i.

Modelled after the ionospheric configuration observed in Figure 1.2, we use six sinusoidals to simulate the differential ionosphere. Figure 3.2 shows the ionosphere used in subsequent estimation experiments.

3.1.3. Azimuth ground movement

The differential azimuth ground motion is simulated as field $G(x,y)$, where each value represents the azimuth offset between reference and secondary observation in meters. G is modelled after the glacial displacement characteristics described by Figure 1.1. To this end, an approach based on the rasterization of Bézier curves is implemented. The glacial flow shape is specified by a Bézier curve $\boldsymbol{b}_r(t) = [b_x(t),\, b_y(t)]^T$ in relative coordinates, such that the curve remains within in the unit square, i.e. $\boldsymbol{b}_r(t) \in [0,1]^2$, $0 \le t \le 1$. The curve is then scaled to the simulated scene's extent and each pixel crossed by the curve is assigned the closest point on the curve to obtain the rasterized curve $R(x,y)$:

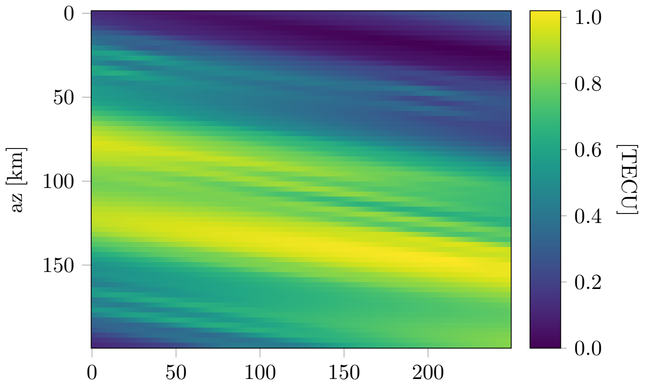

Figure 3.2.: Simulated ionospheric state, resembling a plausible ionospheric configuration over Greenland.

$$R(x,y) = R_{max} \cdot \begin{cases} \underset{t \in \hat{\mathfrak{t}}}{\operatorname{argmin}} \|\boldsymbol{b}_i(t) - \boldsymbol{p}\| & \text{if curve within pixel} \\ 0 & \text{else,} \end{cases} \tag{3.3}$$

with factor R_{max} to scale the curve parameter t, the pixel $\boldsymbol{p} = [x,y]^T$, the Bézier curve $\boldsymbol{b}_i(t) = [({}^{l_{rg}}/{}_{p_{rg}} - 1) \cdot b_x(t), ({}^{l_{az}}/{}_{p_{az}} - 1) \cdot b_y(t)]^T$ in image coordinates and $\hat{\mathfrak{t}} = \{0 \leq t \leq 1 : \|\mathbf{b}_i - \boldsymbol{p}\|_\infty \leq 0.5\}$ being the curve segment overlapping the pixel. We use the parameters in section A.2 and repeat the resulting rasterized offset field in range direction to simulate a glacier that spans one-tenth of the width of the observed ground scene:

$$G(x,y) = \sum_{dx=0}^{w_r-1} R(x+dx), \tag{3.4}$$

with $w_r = \lfloor {}^{w}/{}_{10} \rceil$. The resulting simulated glacier motion is shown in Figure 3.3.

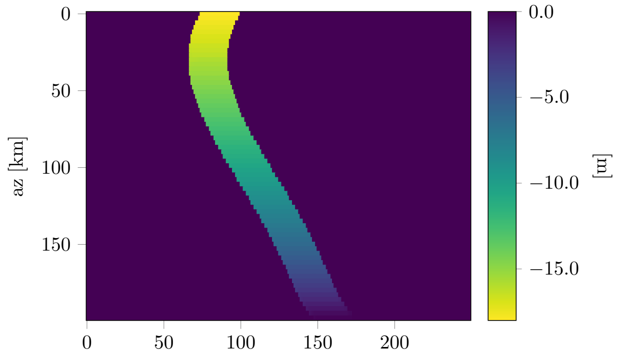

Figure 3.3.: Simulated glacial azimuth ground motion. The glacial shape is modelled after the Petermann Glacier. The maximum azimuth motion between the InSAR pair is assumed to be 18 m in negative azimuth direction.

3.1.4. Split-spectrum measurements

For simplicity of notation, we omit the explicit dependence of $I(x, y)$ and other fields on the spatial coordinates and henceforth denote it simply as I, unless otherwise specified. The measurements obtained by the split-spectrum method I_{ss} are simulated by adding white Gaussian noise $\epsilon_{ss} \sim \mathcal{N}(0, \sigma_{ss}^2)$ to the ionosphere.

$$I_{ss}(x, y) = I_{ss} = I + \epsilon_{ss}. \tag{3.5}$$

The split-spectrum estimation noise as a function of coherence γ, number of looks L, center frequency f_0 and bandwidth B is given in [Gom16] as

$$\sigma_{ss} = \frac{3f_0}{4B}\sqrt{\frac{3}{L}}\frac{\sqrt{1-\gamma^2}}{\gamma} \; [rad]. \tag{3.6}$$

For the parameters in Table 3.1, taking *NISAR* as an example, and with the number of looks approximated as $L = L_{az} \cdot L_{rg} = 2p_{az}/D \cdot 2Bp_{rg}\sin(\alpha)/c \approx 42\,882$, the split-spectrum estimation noise is $\sigma_{ss} \approx 5.26 \times 10^{-1}$ rad $= 3.91 \times 10^{-2}$ TECU.

3.1.5. Azimuth subbands

As explained in subsection 2.4.2, the phase difference observed in the azimuth subbands is comprised of the ionospheric component and azimuth ground motion. In this section, the simulation of the azimuth subbands and the consecutive computation of the azimuth derivative is explained in detail.

Ionosphere Recall the observation geometry of the azimuth subbands as explained in subsection 2.4.2. The distance between sub-aperture centers and the original aperture center along the flight path is $dy_{orb,2} = D_{syn}/4$ for two azimuth subbands and $dy_{orb,3} = D_{syn}/3$ for three azimuth subbands. The corresponding ionospheric pierce points are hence offset by $dy_{iono} = dy_{orb} \cdot H_i/H$. Subbands observing the same ground footprint are affected by different regions of ionosphere, separated in flight-direction by the subband aperture width. The subband geometry is visualized in Figure 3.4.

In the simulation, the different observed ionosphere of the subbands is treated as a shift of the observable ionosphere $I(x, y)$, e.g. for the backward-looking subband

$$S_{iono,+}(x, y) = I(x, y + \tilde{dy}_{img}) \tag{3.7}$$

Due to the shifts, the top and bottom boundary rows are undefined and will be discarded for the subsequent estimation. The physical distance of the sub-aperture centers projected to the height of the ionospheric layer is converted into image coordinates, i.e. $dy_{img} = dy_{iono}/p_{az}$. To avoid resampling we round to the nearest integer shift $\tilde{dy}_{img} = \lfloor dy_{img} \rceil$. The rounding can be interpreted as selecting the closest ionospheric height to H_i leading to an integer shift: $\tilde{H}_i = \tilde{dy}_{img} p_{az} H/dy_{orb}$.

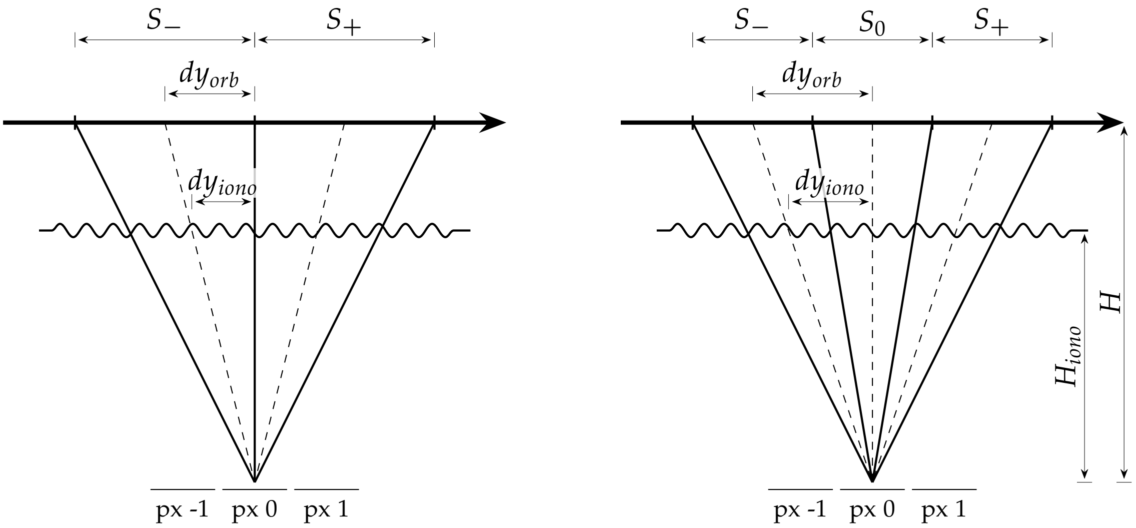

(a) 2 azimuth subbands

(b) 3 azimuth subbands

Figure 3.4.: Geometry for two and three azimuth subbands.

Subband shift examples For the ionospheric height of $H_i = 350\,\mathrm{km}$ and *NISAR* parameters, the synthetic aperture is $D_{syn} \approx 19\,381\,\mathrm{km}$, the offset of azimuth subbands $dy_{orb,2} \approx 5\,\mathrm{km}$. The shift in image pixels is then $\tilde{dy}_{img,2} = \lfloor 1 \rceil = 1$, i.e. the ionosphere observed by the azimuth subbands is simulated by shifting the ionosphere by one pixel in positive and negative azimuth direction respectively. For three subbands, $\tilde{dy}_{img,3} = \lfloor 1 \rceil = 1$, where the center subband is taken as an unaltered copy of the ionosphere $I(x,y)$. A complete list of resulting shift quantities is found in Table 3.2.

Subband phase noise Each subband is subject to phase noise $S_\sigma \sim \mathcal{N}(0, \sigma_S^2)$, which is simulated as random Gaussian noise superimposed to the ionospheric phase screen. With N subbands, the number of looks L and coherence γ, the variance is given in [SC94] as

$$\sigma_S^2 = \frac{N}{2L}\frac{1-\gamma^2}{\gamma^2}\ [rad^2] = \left(\frac{cf_0}{4\pi K}\right)^2 \frac{N}{2L}\frac{1-\gamma^2}{\gamma^2}\ [TECU^2]. \tag{3.8}$$

Azimuth ground movement Due to the squinted geometry, each subband's phase difference contains a contribution of the azimuth ground motion between acquisitions. With the azimuth ground motion G in meters, orbit velocity v and the subband's doppler centroid frequency $f_{D,S}$, the ground motion contribution is

$$S_{mov,+}(x,y) = 2\pi f_{D,+}\frac{G(x,y)}{v}. \tag{3.9}$$

quantity		**values**				
		2 subbands		3 subbands		
		S_-	S_+	S_-	S_0	S_+
dy_{orb}	[m]	−4845	4845	−6460	0	6460
dy_{iono}	[m]	−2270	2270	−3027	0	3027
dy_{img}	[px]	−0.76	0.76	−1.01	0.0	1.01
$\tilde{dy}_{img}$	[px]	−1	1	−1	0	1
$\tilde{dy}_{img}$	[km]	463		347		

Table 3.2.: Subband azimuth offsets for all subbands for the configurations of two and three azimuth subbands respectively.

Azimuth derivative Each subband is then the sum of the shifted ionosphere's influence, the ground motion contribution and random phase noise:

$$\begin{aligned} S_- &= S_{iono,-} + S_{mov,-} + S_{\sigma,-} \\ S_+ &= S_{iono,+} + S_{mov,+} + S_{\sigma,+} \\ S_0 &= S_{iono,0} + \underbrace{S_{mov,0}}_{=0} + S_{\sigma,0} \end{aligned} \tag{3.10}$$

where S_+ denotes the backward-looking azimuth subband, S_- the forward-looking subband and S_0 the optional center subband. Note that the simulation of subbands depends on the number of azimuth subbands. We refrain from using an explicit index to avoid overloading the notation. Also, the differences are scaled by the respective grid resolution, which is not indicated in the following equations for simplicity.

Finally, the difference between subbands is formed. For the configuration of two azimuth subbands, we compute a single difference between the backward-looking subband and forward-looking subband i.e.

$$\delta I_{az,2} = S_+ - S_- \tag{3.11}$$

For three azimuth subbands, we determine the double difference of the two squinted subbands and the broadside subband:

$$\delta I_{az,3} = S_+ - 2S_0 + S_- \tag{3.12}$$

3.2. Estimation

This section describes the implementation details of the estimation from multiple measurement sources. First, the general framework of Bayesian estimation is described, followed by a detailed description of the input data and their associated uncertainties, as well as the regularization.

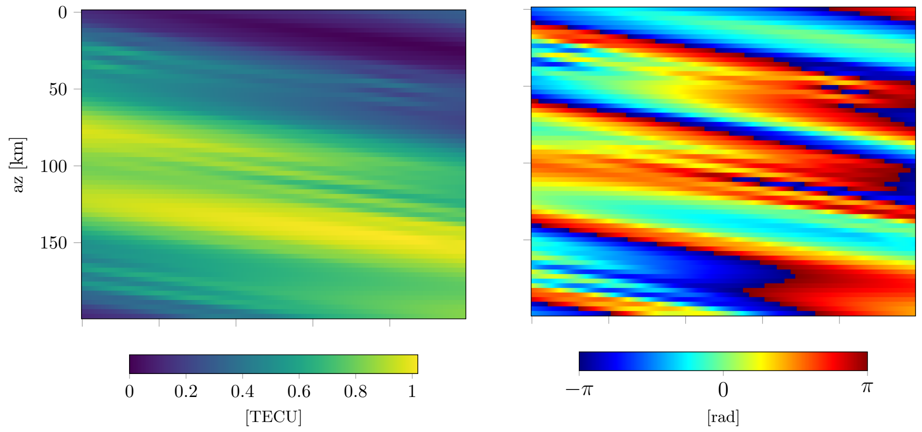

(a) Ionosphere (b) Interferogram

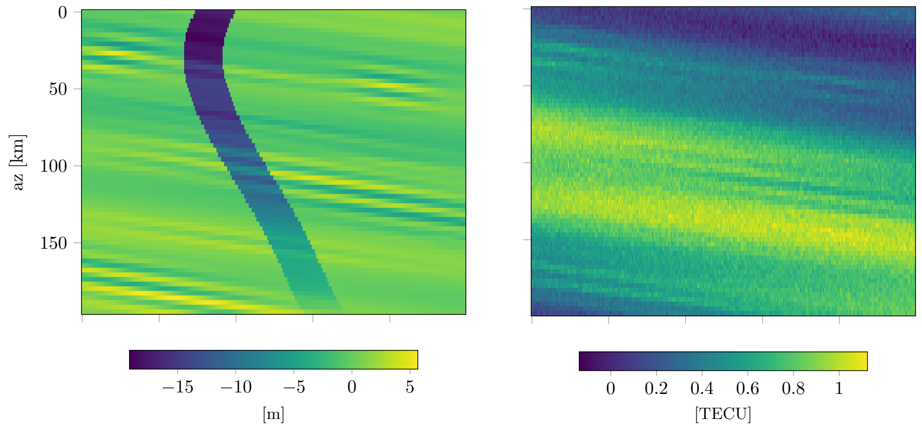

(c) Azimuth shifts (d) Split-spectrum

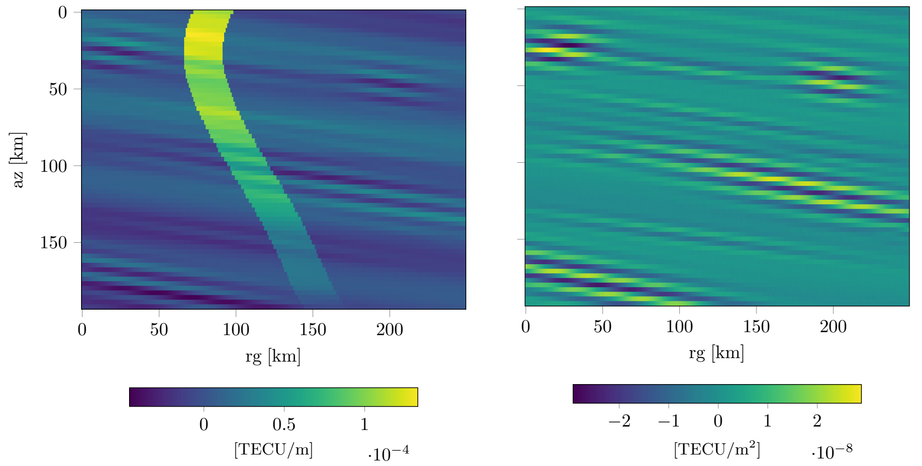

(e) First derivative (f) Second derivative

Figure 3.5.: Input data to the estimation. **(a)** ionosphere modelled to resemble a typical scintillation in polar regions **(b)** interferometric phase caused by ionosphere **(c)** azimuth shifts as caused by linear variations of the ionosphere in azimuth direction and superimposed by azimuth motion of the ground **(d)** simulated split-spectrum estimate **(e)** discrete first derivative of azimuth phase history, computed from simulated azimuth subbands **(d)** second derivative of azimuth phase history

3.2.1. Bayesian inversion

The ionosphere estimation is formulated as a Bayesian inversion problem, allowing for measurements of multiple sources and prior information to be combined to obtain a posterior estimate of the ionospheric state. The measurement vector $\boldsymbol{y}$ is comprised of ionosphere estimates obtained using the split-spectrum method $\boldsymbol{y}_{ss}$ and optionally additional observations $\boldsymbol{y}_{az,S}$ computed from the S azimuth subbands. The forward problem is

$$\boldsymbol{y} = \boldsymbol{D}\boldsymbol{x} + \boldsymbol{\epsilon}, \tag{3.13}$$

with the measurement vector $\boldsymbol{y} = [\boldsymbol{y}_{ss}^T, \boldsymbol{y}_{az}^T]^T = [y_0, \dots, y_m]^T$, the model matrix $\boldsymbol{D}$ and measurement noise vector $\boldsymbol{\epsilon}$. The vector $\boldsymbol{x} = [x_0, \dots, x_n]^T$ holds the $n = h \cdot w$ values of the flattened 2D ionosphere. The parameters $\boldsymbol{x}$ and noise $\boldsymbol{\epsilon}$ are assumed to be normally distributed, i.e. $\boldsymbol{x} \sim \mathcal{N}(x_0, \boldsymbol{C_{xx}})$ and $\boldsymbol{\epsilon} \sim \mathcal{N}(\boldsymbol{0}, \boldsymbol{C_{\epsilon\epsilon}})$.

The maximum a posteriori estimate $\hat{\boldsymbol{x}}$ is obtained by

$$\hat{\boldsymbol{x}} = \boldsymbol{x}_0 + (\boldsymbol{D}^T\boldsymbol{C}_{\epsilon\epsilon}^{-1}\boldsymbol{D} + \boldsymbol{C}_{\boldsymbol{xx}}^{-1})^{-1}\,\boldsymbol{D}^T\boldsymbol{C}_{\epsilon\epsilon}^{-1}\,(\boldsymbol{y} - \boldsymbol{D}\boldsymbol{x}_0) \tag{3.14}$$

3.2.2. Input data

The data generation process was explained in section 3.1. Figure 3.5 shows the simulated 2D data used in the estimation experiments. This section highlights the implementation details of the estimation and the involved quantities.

Measurement vectors The simulation of the split-spectrum estimate data I_{ss} and the azimuth subband data δI_{az} is explained in subsection 3.1.4 and subsection 3.1.5. For the estimation, both data matrices are flattened into vectors $\boldsymbol{y}_{az} \in \mathbb{R}^n$ and $\boldsymbol{y}_{ss} \in \mathbb{R}^{n_{az}}$.

Noise covariance Each singular subband is subject to phase noise σ_S^2 as specified in Equation 3.8. The noise of the derivative as a linear combination of the random variables scaled by the difference coefficients is:

$$\sigma_{az}^2 = \begin{cases} \left(\frac{-0.5}{p_{az}}\right)^2 \sigma_S^2 + \left(\frac{0.5}{p_{az}}\right)^2 \sigma_S^2 & \text{for two subbands} \\ \\ \left(\frac{1}{p_{az}^2}\right)^2 \sigma_S^2 + \left(\frac{-2}{p_{az}^2}\right)^2 \sigma_S^2 + \left(\frac{1}{p_{az}^2}\right)^2 \sigma_S^2 & \text{for three subbands} \end{cases} \tag{3.15}$$

The measurement noise is assumed to be uncorrelated, hence the corresponding covariance matrix is diagonal with the respective noise variances of the split-spectrum measurements and azimuth derivative measurements:

$$\boldsymbol{C_{\epsilon\epsilon}} = \text{diag}(\underbrace{\sigma_{ss}^2, \dots, \sigma_{ss}^2}_{n}, \underbrace{\sigma_{az}^2, \dots, \sigma_{az}^2}_{n_{az}}).$$

For the split-spectrum only case, the noise covariance is comprised of the split-spectrum variance only.

Prior covariance The prior covariance matrix may be used to incorporate prior knowledge about the spectrum of the ionosphere signal. Assuming a smooth ionosphere with respect to the raster resolution, $\boldsymbol{C}_{\boldsymbol{xx}}$ may regularize the inversion and enforce a smooth solution of the estimate. [Rin79] defines a physically realistic covariance of the Matérn family that can model turbulent ionospheric effects at the equator. In [GD17], it is used to represent the spectrum of general turbulent effects and is estimated from the split-spectrum measurements after detrending. For the sake of simplicity and in order to test the estimation performance of the different methods under idealized conditions, we assume the prior spectral characteristics to be well-known. To this end, we utilize the autocorrelation of the true ionosphere as the prior covariance Assuming wide-sense stationarity, the autocorrelation holds spectral information about the estimation target. Estimating the prior covariance from the split-spectrum measurements instead of the true ionosphere has shown to have a negligible effect on the estimation quality at the chosen resolution. The autocorrelation in its flattened form then corresponds to one row of the prior covariance matrix and is repeated for each parameter x_i.

Model matrix The model matrix $\boldsymbol{D}$ is a comprised of the sub-matrices for the measurements, i.e.

$$\boldsymbol{D} = \boldsymbol{D}_{ss} \qquad \text{or} \qquad \boldsymbol{D} = \begin{bmatrix} \boldsymbol{D}_{ss} \\ \boldsymbol{D}_{az} \end{bmatrix}, \tag{3.16}$$

with $\boldsymbol{D}_{az}$ being the discrete azimuth derivative operator for the respective subband geometry. $\boldsymbol{D}_{az}$ contains the coefficients of central difference quotients, with stencil points equivalent to $\tilde{dy}_{img}$. The model matrix is designed in the flattened geometry, hence the coefficients lie on off-diagonals corresponding to the azimuth neighbors.

3.3. Experiments

We conduct the following experiments to determine the feasibility of improving the estimation and compensation of ionospheric effects by the introduction of derivative information: estimation from split-spectrum estimates alone (SS), split-spectrum in combination with the azimuth derivative from two azimuth subbands (SS+AZ2) and split-spectrum together with the second azimuth derivative from three azimuth subbands (SS+AZ3).

First, we present the raw split-spectrum estimates as a baseline. Building on the raw estimates, we add regularization to filter the noise and analyze how the regularization affects the residuals. For the case SS+AZ2 and SS+AZ3, both regularized and non-regularized results are presented. We observe the residual interferometric phase and residual azimuth shifts as indicators of the estimation quality and compare the methods by computing the root mean square (RMS) of the residual quantities.

4. Results

This chapter presents the outcomes of estimations with different sets of input data. The first results correspond to the case of superimposed azimuth ground motion and ionosphere. We present a visual analysis of the compensated interferograms and residual azimuth shifts, as well as their RMS. Note, that the colorbar of the residual azimuth shifts is fixed to the scale of *SS (regularized)*, to ensure comparability. We repeat the experiment *SS+AZ2* for a situation without azimuth ground motion. Numerical results are presented in Table 4.1 for estimations under azimuth motion and Table 4.2 in the absence of ground motion.

4.1. With azimuth ground motion

In this section, the ionosphere estimation was performed under the influence of azimuth ground motion. We compare the estimation via *SS*, *SS+AZ2* and *SS+AZ3*.

Split-Spectrum

No regularization Without regularization, the output of the Bayesian inversion is equivalent to the input (the split-spectrum measurement), and hence subject to strong phase noise. This experiment serves as the baseline, motivating further improvement of the estimation. The high-frequency noise causes a residual phase in the interferogram of up to 2.14 rad. The non-compensated ionosphere introduces azimuth shifts of up to 6.71 m. The results confirm, that the split-spectrum estimate needs to be filtered to reduce the estimation noise.

With regularization After introducing regularization to the estimation, the phase noise can be largely reduced to 0.75 rad. On the flip side, high-frequency ionospheric components are filtered and contribute to residual azimuth shifts, which remain substantial with 1.84 m in high-frequency areas and 0.35 m overall.

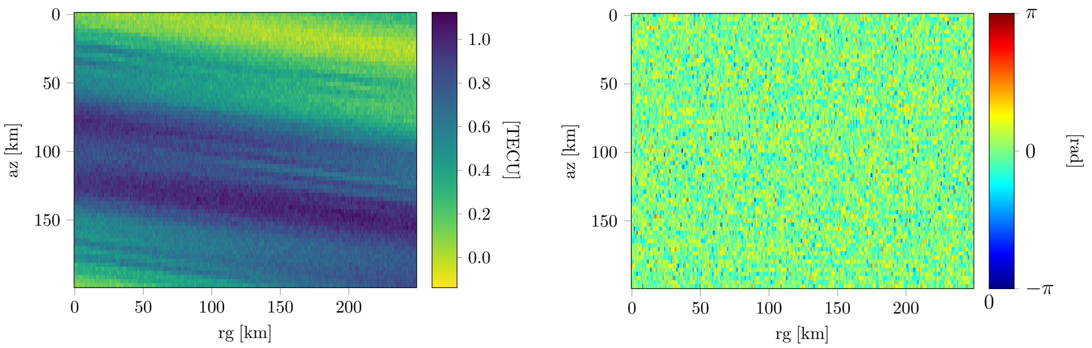

(a) Estimated ionosphere

(b) Residual interferometric phase

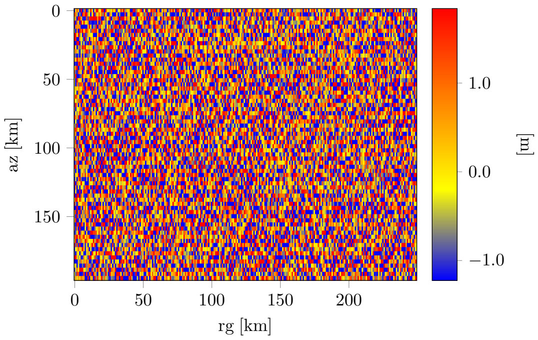

(c) Residual ionospheric azimuth shifts

Figure 4.1.: Estimation results using only split-spectrum measurements and no regularization.

Split-Spectrum + 2 Azimuth Subbands

No regularization The introduction of derivative information to the estimation is expected to contribute to the recovery of high-frequency ionospheric components, with the drawback of being biased by azimuth ground motion. The unregularized estimation, however, suffers from strong artifacts in azimuth direction, which can be reduced by regularizing by means of a prior covariance model.

With regularization The results of the estimation confirm the expectation, as the ionosphere estimate is heavily disturbed by the ground motion contribution to the first derivative of the azimuth phase history. Converted to interferometric phase, the errors span multiple phase cycles, as can be seen in the compensated interferogram in Figure 4.4. Further, the azimuth shifts of the estimated ionosphere are dominated by the contribution of the azimuth ground motion, increasing the maximum error to 17.98 m and the RMS error to 2.30 m. Some estimation artifacts can still be observed, but are not the main source of error.

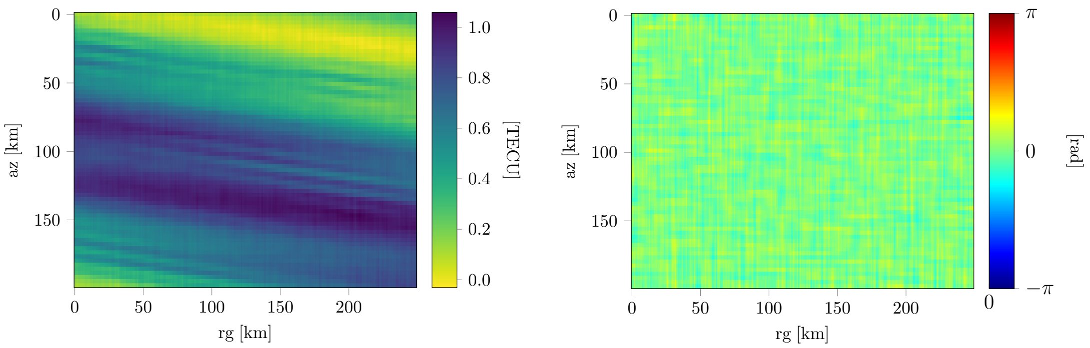

(a) Estimated ionosphere (b) Residual interferometric phase

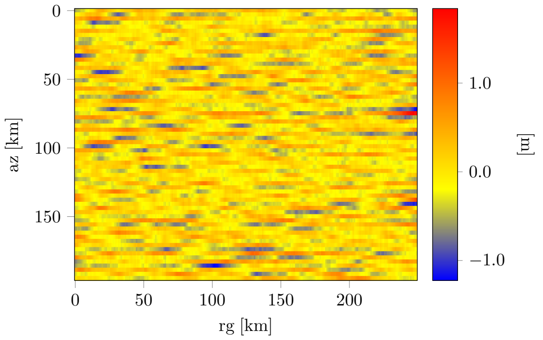

(c) Residual ionospheric azimuth shifts

Figure 4.2.: Estimation results of regularized *SS*.

Split-Spectrum + 3 Azimuth Subbands

As shown in Equation 2.10, using the second derivative of the azimuth phase history allows to separate ionosphere and azimuth ground motion. Here, we present the results of an estimation combining split-spectrum measurements with measurements of the second derivative. The estimation of the ionospheric phase screen using *SS+AZ3* outperforms the previous approaches. Compared to *SS*, the method better recovers the high-frequencies of the ionosphere and does not suffer from a bias caused by ground motion as for *SS+AZ2*. The RMS interferometric phase error is 0.12 rad and the residual RMS shift to 0.05 m, a reduction of factor six with respect to *SS (regularized)* and factor 40 with respect to the biased *SS+AZ2 (regularized)*.

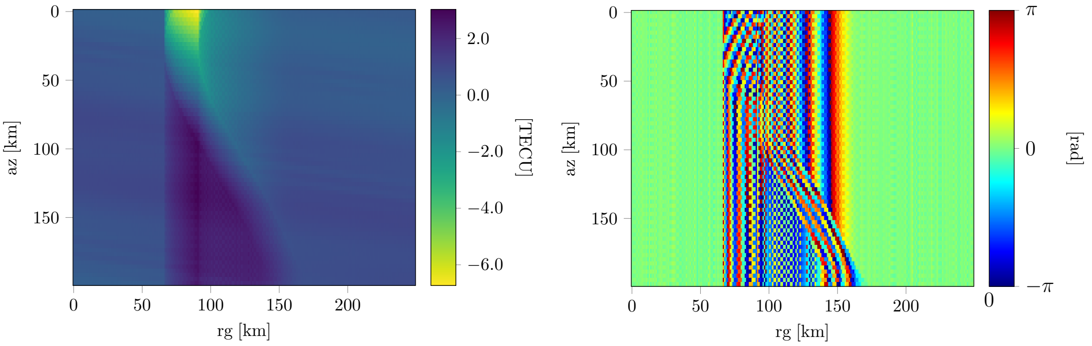

(a) Estimated ionosphere

(b) Residual interferometric phase

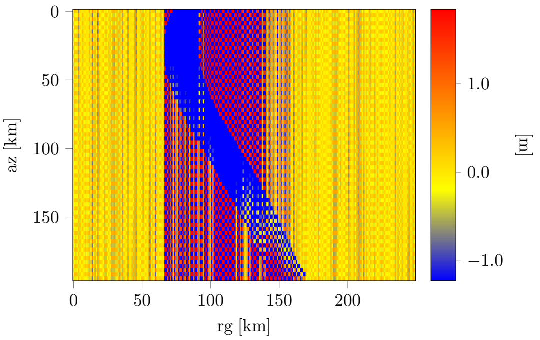

(c) Residual ionospheric azimuth shifts

Figure 4.3.: Estimation results using split-spectrum measurements in combination with the first azimuth derivative. No prior covariance for regularization is applied.

4.2. No azimuth ground motion

The split-spectrum measurements are independent of azimuth ground motion, therefore the estimation results are equal to those above. As shown before, the same applies to the estimation with SS+AZ3. Only for SS+AZ2, the results differ and are presented here.

The results show that the derivative information from two subbands suffices to recover high-frequency ionosphere in the absence of azimuth ground motion. The estimation also experiences some artifacts, but the overall phase error is reduced to 0.28 rad.

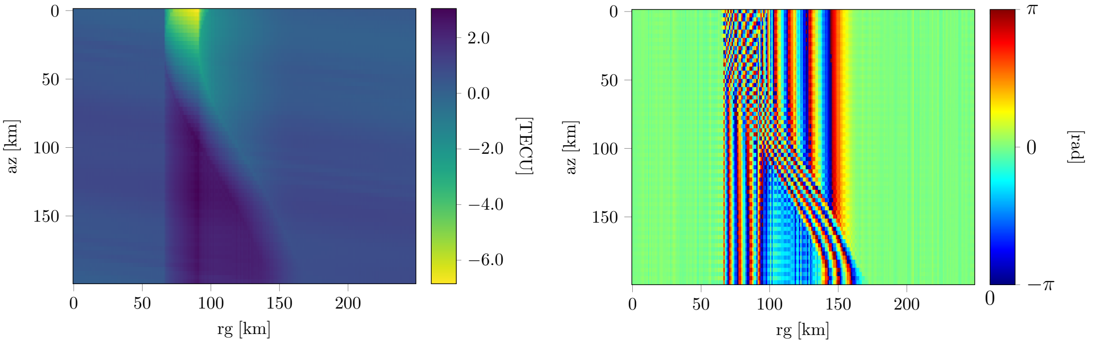

(a) Estimated ionosphere

(b) Residual interferometric phase

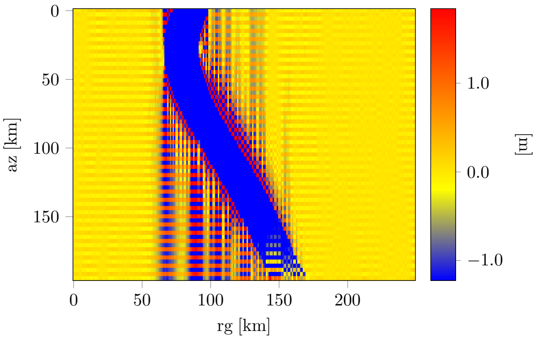

(c) Residual ionospheric azimuth shifts

Figure 4.4.: Regularized estimation results using split-spectrum and the first derivative.

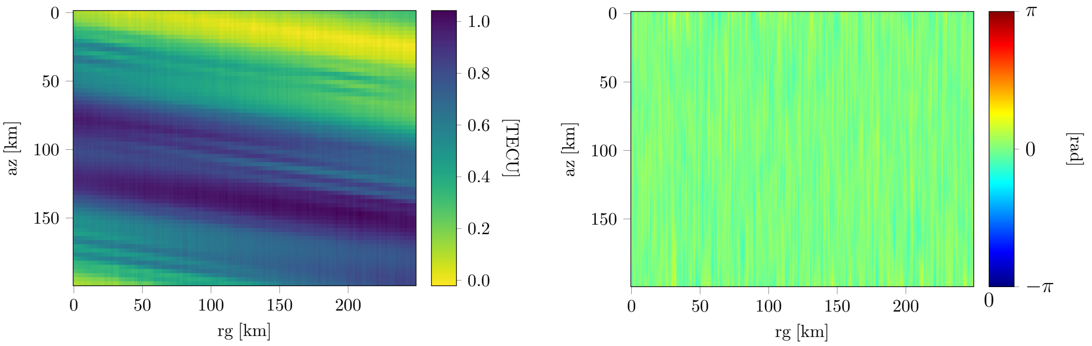

(a) Estimated ionosphere

(b) Residual interferometric phase

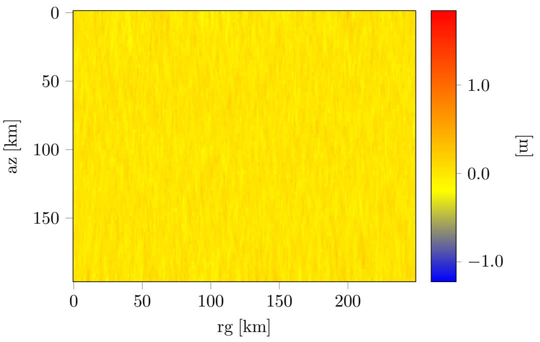

(c) Residual ionospheric azimuth shifts

Figure 4.5.: Estimation results using split-spectrum measurements and the second azimuth phase derivative from three subbands, regularized.

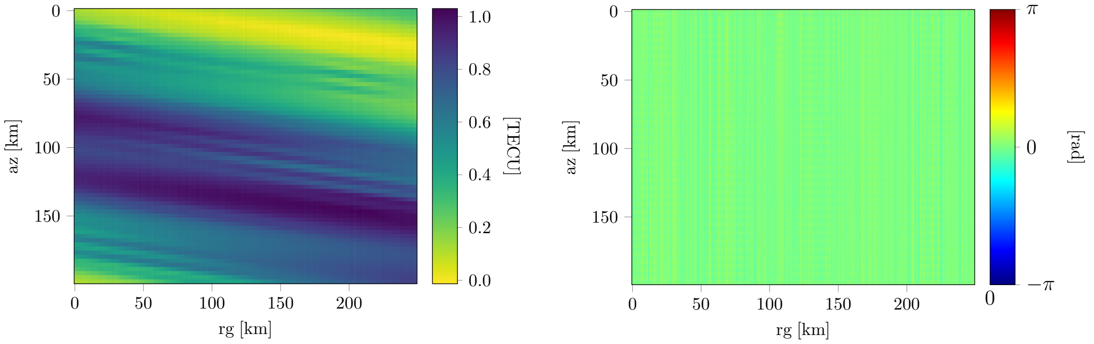

(a) Estimated ionosphere

(b) Residual interferometric phase

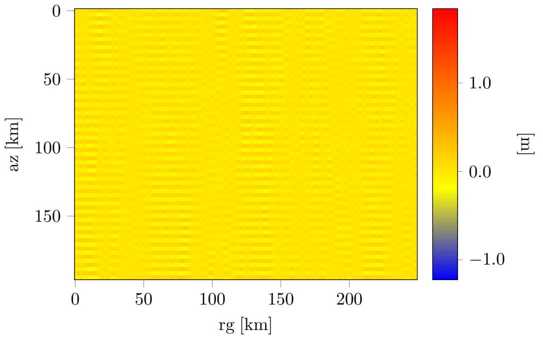

(c) Residual ionospheric azimuth shifts

Figure 4.6.: Estimation with the first derivative added to the measurements, assuming no azimuth ground motion is present.

data	**regularized**	**interf. phase** [rad]		**az. shifts** [m]	
		rms	factor	rms	factor
SS	False	0.525	4.324	1.647	32.114
SS	True	0.172	1.413	0.347	6.765
SS+AZ2	False	1.099	9.049	3.124	60.930
SS+AZ2	True	1.078	8.882	2.299	44.838
SS+AZ3	False	0.151	1.246	0.070	1.361
SS+AZ3	True	**0.121**		**0.051**	
SS+AZ23	True	1.073	8.838	2.100	40.955

Table 4.1.: Experiments with azimuth ground motion present. Root mean squared error (rms) and relative factors to the best method of the residual interferometric phase and the residual azimuth shifts.

data	**regularized**	**interf. phase** [rad]		**az. shifts** [m]	
		rms	factor	rms	factor
SS	False	0.525	8.229	1.647	32.115
SS	True	0.172	2.690	0.347	6.765
SS+AZ2	False	0.094	1.470	0.305	5.958
SS+AZ2	True	**0.064**		0.069	1.336
SS+AZ3	False	0.151	2.371	0.070	1.361
SS+AZ3	True	0.121	1.903	**0.051**	

Table 4.2.: Experiments without azimuth ground motion present. Root mean squared error (rms) and relative factors to the best method of the the residual interferometric phase and the residual azimuth shifts.

5. Conclusion

Summarizing the thesis, we evaluated the use of azimuth subbands for the improved estimation of the ionosphere from SAR data, more specifically from InSAR pairs. We established how current state-of-the-art methods struggle to achieve the spatial resolution required to fully compensate ionospheric azimuth shifts. Based on the idea of data combination, the thesis shows how two azimuth subbands can be used to recover the ionosphere if no azimuth ground motion between the observations biases the estimation. Extending the method to three subbands allows to recover high-frequency ionosphere even in the presence of azimuth ground motion and reduces the azimuth shifts by a factor of 40 with respect to the biased estimation from two subbands and a factor of 6 compared to a filtered split-spectrum estimation. In future work, implementation details like the reduction of estimation artifacts, memory consumption and estimation runtime would need to be studied in order to operationalize the method. Furthermore, the sensitivity of the method to the prior covariance model should be evaluated, as in this work, the prior is assumed to be well known, providing close-to-optimal regularization. Finally, the method should be tested on real-world data to determine the gain in precision of glacial motion estimation.

A. Simulation parameters

A.1. Ionosphere

We use amplitudes $A_i \in \{0.1,\ 0.01,\ 0.04,\ 0.04,\ 0.4, 0.1\}$ TECU, wavelengths $\lambda_i \in \{50,\ 12,\ 12,\ 250, 11\}$ km and rotations $\theta_i \in \{6,\ 7,\ 7,\ 7,\ 14, 7\}^\circ$ to simulate the ionosphere in this thesis. High-frequency components are only locally faded into the lower-frequency ionosphere.

A.2. Ground Movement

Maximum azimuth motion
$R_{max} = -18\,\mathrm{m}$

Bézier control points center

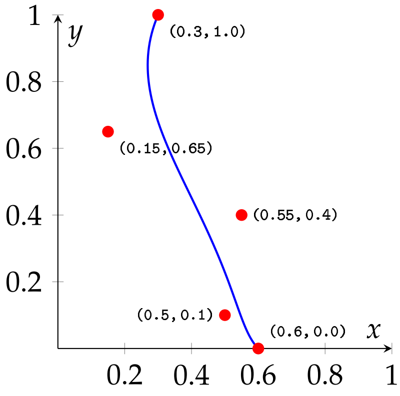

Figure A.1.: Bézier curve (and generating control points) used as flow shape of glacial azimuth displacement
center

A.3. Further results

Maximum residuals are presented alongside the RMS.

data	**regularized**	**interf. phase** [rad]		**az. shifts** [m]	
		rms	maxabs	rms	maxabs
SS	False	0.525	2.139	1.647	6.709
SS	True	0.172	0.753	0.347	1.840
SS+AZ2	False	1.099	3.142	3.124	29.664
SS+AZ2	True	1.078	3.141	2.299	17.978
SS+AZ3	False	0.151	0.782	0.070	0.408
SS+AZ3	True	**0.121**	**0.552**	**0.051**	**0.281**
SS+AZ23	True	1.073	3.141	2.100	14.003

Table A.1.: Experiments with azimuth ground motion present. Root mean squared error (rms) and maximum absolute value (maxabs) of the residual interferometric phase and the residual azimuth shifts.

data	**regularized**	**interf. phase** [rad]		**az. shifts** [m]	
		rms	maxabs	rms	maxabs
SS	False	0.525	2.139	1.647	6.709
SS	True	0.172	0.754	0.347	1.840
SS+AZ2	False	0.094	0.334	0.305	0.875
SS+AZ2	True	**0.064**	**0.248**	0.069	**0.222**
SS+AZ3	False	0.151	0.782	0.070	0.408
SS+AZ3	True	0.121	0.552	**0.051**	0.281

Table A.2.: Experiments without azimuth ground motion present. Root mean squared error (rms) and maximum absolute value (maxabs) of the the residual interferometric phase and the residual azimuth shifts.

List of Figures

List of Tables

Acronyms

InSAR interferometric SAR. 1, 5, 6, 11, 14, 29

LOS line of sight. 6, 7

RMS root mean square. 20, 21, 22

SAR synthetic aperture radar. 1, 5, 29

TEC total electron content. 5, 7

Bibliography

[Brc+10] R. Brcic, A. Parizzi, M. Eineder, et al. "Estimation and compensation of ionospheric delay for SAR interferometry." In: *2010 IEEE International Geoscience and Remote Sensing Symposium*. 2010, pp. 2908–2911.

[BZ06] N. B. D. Bechor and H. A. Zebker. "Measuring two-dimensional movements using a single InSAR pair." In: *Geophysical Research Letters* 33.16 (2006).

[Dav90] K. Davies. *Ionospheric Radio*. 1990.

[End+14] E. M. Enderlin, I. M. Howat, S. Jeong, et al. "An improved mass budget for the Greenland ice sheet." In: *Geophysical Research Letters* 41.3 (2014), pp. 866–872.

[Fox+21] B. Fox-Kemper, H. Hewitt, C. Xiao, et al. "Ocean, Cryosphere and Sea Level Change." In: *Climate Change 2021: The Physical Science Basis. Contribution of Working Group I to the Sixth Assessment Report of the Intergovernmental Panel on Climate Change*. 2021. Chap. 9, pp. 1211–1361.

[GD17] G. Gomba and F. De Zan. "Bayesian Data Combination for the Estimation of Ionospheric Effects in SAR Interferograms." In: *IEEE Transactions on Geoscience and Remote Sensing* 55.11 (2017), pp. 6582–6593.

[Gom] G. Gomba. *Study on Ionospheric Effects on SAR and their Statistics*. Internal report, unpublished.

[Gom+16] G. Gomba, A. Parizzi, F. De Zan, et al. "Toward Operational Compensation of Ionospheric Effects in SAR Interferograms: The Split-Spectrum Method." In: *IEEE Transactions on Geoscience and Remote Sensing* 54.3 (2016), pp. 1446–1461.

[Gom16] G. Gomba. *Estimation and Compensation of Ionospheric Propagation Delay in Synthetic Aperture Radar (SAR) Signals*. Tech. rep. Remote Sensing Technologies Institute, 2016.

[Her+11] M. Hernández-Pajares, J. M. Juan, J. Sanz, et al. "The ionosphere: effects, GPS modeling and the benefits for space geodetic techniques." In: *Journal of geodesy* 85.12 (2011), pp. 887–907.

[Lem+18] A. Lemos, A. Shepherd, M. McMillan, et al. "Ice velocity of Jakobshavn Isbræ, Petermann Glacier, Nioghalvfjerdsfjorden, and Zachariæ Isstrøm, 2015–2017 from Sentinel 1-a/b SAR imagery." In: *The Cryosphere* 12.6 (2018), pp. 2087–2097.

[Lia+24] C. Liang, E. J. Fielding, Z. Liu, et al. "An analysis of the potentials of L-band SAR satellites for measuring azimuth motion." In: *Remote Sensing of Environment* 315 (2024), p. 114426.

[RHC10] P. A. Rosen, S. Hensley, and C. Chen. "Measurement and mitigation of the ionosphere in L-band Interferometric SAR data." In: *2010 IEEE Radar Conference*. 2010, pp. 1459–1463.

[Rin79] C. L. Rino. "A power law phase screen model for ionospheric scintillation: 1. Weak scatter." In: *Radio Science* 14.6 (1979), pp. 1135–1145.

[SC94] M. Seymour and I. Cumming. "Maximum likelihood estimation for SAR interferometry." In: *Proceedings of IGARSS '94 - 1994 IEEE International Geoscience and Remote Sensing Symposium*. Vol. 4. 1994, 2272–2275 vol.4.

[She+12] A. Shepherd, E. R. Ivins, G. A, et al. "A Reconciled Estimate of Ice-Sheet Mass Balance." In: *Science* 338.6111 (2012), pp. 1183–1189.